ACS Sustainable Chemistry & Engineering

Research Article

pubs.acs.org/journal/ascecg

Top-down Strategy toward Versatile Graphene Quantum Dots for Organic/Inorganic Hybrid Solar Cells

Yuancheng Qin,*[,†] Yuanyuan Cheng,[†] Longying Jiang,[‡] Xiao Jin,*[,†] Mingjun Li,[†] Xubiao Luo,[†] Guoqing Liao,[†] Taihuei Wei,[§] and Qinghua Li*[,†]

[†]Key Laboratory of Jiangxi Province for Persistent Pollutants Control and Resources Recycle, Nanchang Hangkong University, Fenghenan Street, Nanchang 330063, People's Republic of China

[‡]Xiamen Knano Graphene Technology Co. Ltd., Dongfu Road, Xiamen 361001, People's Republic of China

[§]Department of Physics, National Chung-Cheng University, Daxue Road, Chia-Yi 621, Taiwan, Republic of China

Supporting Information

ABSTRACT: Metal oxide nanocrystals have been pursued for various applications in photovoltaics as a buffer layer. However, it remains a challenging task to adjust their energy levels to achieve a better match of the donor−acceptor system. Herein, we report the fabrication of graphene quantum dots (GQDs) with bright blue photoluminescence by a top-down strategy based on laser fragmentation with posthydrothermal treatment. The GQDs demonstrate appropriate energy level positions and are used as an intermediate buffer layer between TiO_2 and P3HT to form a cascade energy level architecture. The introduction of the GQDs into a bulk heterojunction hybrid solar cell has led to an enhancement of the power conversion efficiency.

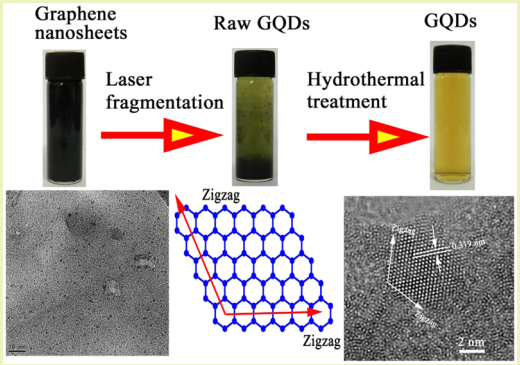

KEYWORDS: *Organic/inorganic solar cells, graphene, carbon quantum dots, top-down, buffer layer*

INTRODUCTION

Bulk heterojunctions (BHJ) based on blends of conjugated polymer donors and inorganic acceptors are one of the most promising candidates for the fabrication of low-cost solar cells to meet the clean-energy demands of the twenty-first century.[1] This type of solar cells possesses unique advantages of the both components such as low-temperature processing of organic semiconductors and high dielectric constant of inorganic semiconductors.[2−4] Over the past 5 years, the organic−inorganic hybrid solar cells (HSCs) based on a well-known poly(3-hexylthiophene) (P3HT) have suffered low power conversion efficiency (PCE) abilities, most of which range from 1.0 to 3.0%, depending on the activities of the inorganic semiconductors such as their types, morphologies, electronic properties and others applications.[5−8] Many efforts have been made aiming to improve the performances of HSCs, such as modifying the size and morphologies of the inorganic semiconductors,[4,9] tuning the electronic structure by ion doping,[10,11] and utilizing low band gap organic materials[12] or introducing buffer layers.[13−16] Among these, incorporating an intermediate layer has attracted much attention. The intermediate layer can acts as a blocking media that hinders the flow of photoexcited electrons to the back contact or prevents geminate recombination of electron−hole pairs from the active layer at the back boundaries.[17−20] Besides, the insertion of an intermediate layer can give a rise in reactions between the donor and the acceptor, thus reducing the barrier at the interface.[21] Furthermore, a buffer layer with an appropriate absorption range can also cooperate with organic semiconductors to achieve a better match of the solar spectrum and to enhance spectral coverage, and finally ameliorate the device performances.[22,23]

Metal oxide nanocrystals such as MoO_3,[21,24−26] V_2O_5[22,27−29] and ZnO[14,30,31] have been widely used as buffer layers, owing to their high work function or good conductivity. Previous works mainly focus on either the blocking effects or the charge transfer resistance. Nevertheless, the origin of the intrinsic driving force behind the excellent performances remains unknown, especially the energy level re-engineering effects are rarely involved. The present organic−inorganic HSCs based on P3HT can absorb a large amount of solar light due to their small bandgap (∼1.9 eV), whereas the PCEs are far below their absorption ability due to the initial cooling of the hot excitons or insufficient separation of electron−hole pairs. In previous studies, we have demonstrated that the energy formation between the donor and acceptor plays an important role in charge transfer rate at the interface of the BHJ.[32−34] Therefore, a promising way to enhance the PCE lies in the intermediate layer with appropriate electronic activity to gain energy level matching between donor and acceptor. However, metal oxide

Received: December 1, 2014
Revised: January 26, 2015
Published: February 17, 2015

ACS Publications © 2015 American Chemical Society

DOI: 10.1021/sc500761n
ACS Sustainable Chem. Eng. 2015, 3, 637−644

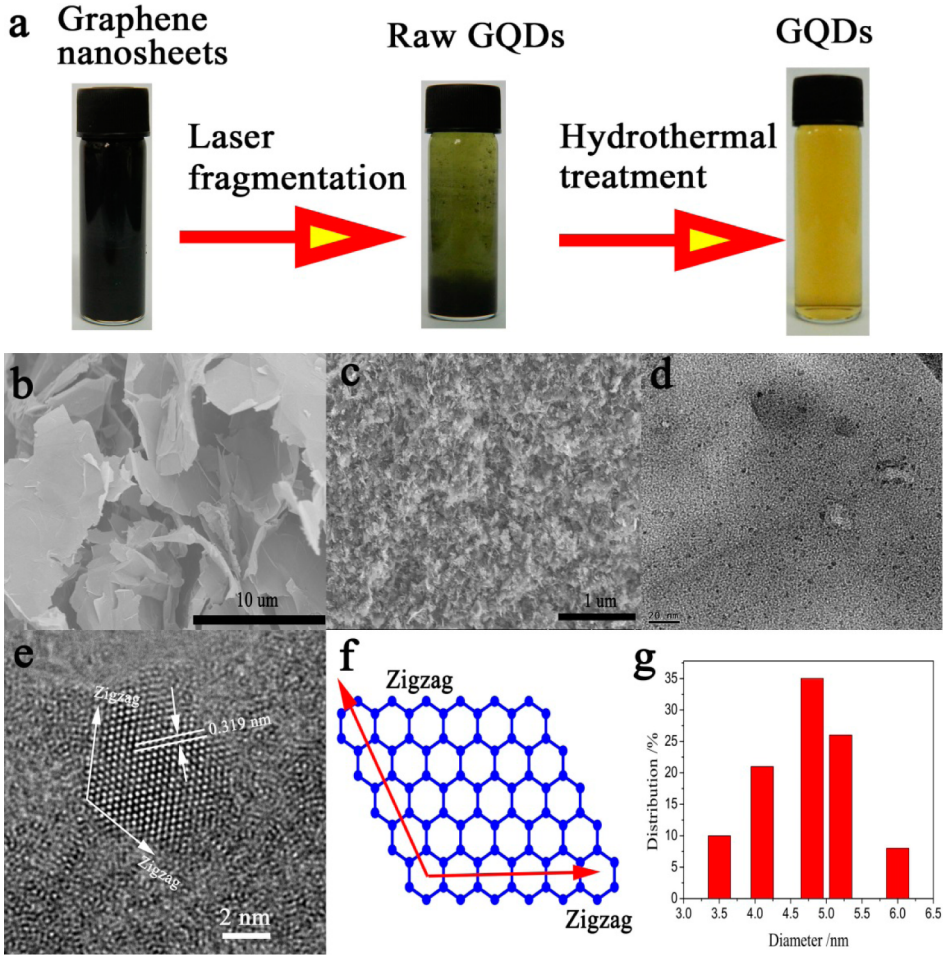

Figure 1. (a) Photos of the graphene nanosheet solution target (left), after laser fragmentation (middle) and the raw GQDs after hydrothermal treatment (right). (b) SEM image of the graphene nanosheet. (c) SEM image of the raw GQDs. (d) TEM image of the GQDs. (e) High-resolution TEM image of the individual GQDs. (f) Orientation of the hexagonal GQDs network and the relative zigzag directions. (g) Histogram of diameter distribution.

semiconductors are impotent in adjusting their energy level by controlling synthesis techniques. Yet, most of them are deposited using cost-intensive vacuum techniques that are incompatible with low-cost solution processable HSCs.

Metal QD semiconductors have attracted a lot of attention for photovoltaic (PV) applications.[35−37] However, only a few of the available metal QD semiconductor materials such as II-VI and [38] IV-VI[39,40] have been exploited thus far, which restricts the continuing success of photonic technologies. Recently, graphene quantum dots (GQDs) have inspired extensive studies on them due to their great potential for a wide variety of technical applications.[41−46] GQDs have exhibited tunable fluorescence emission or electronic properties and low charge transfer resistance,[44] which enable their potential applications in HSCs as a buffer layer. Moreover, GQDs have advantages in low toxicity, biocompatibility, low cost and chemical inertness compared with metal oxide nanocrystals.[43] This prompts us to replace metal oxide with GQDs as a buffer layer for HSC applications. In this work, we report on a hydrothermal top-down routine for fluorescence tunable GQDs and the improvement of the photovoltaic properties of the HSCs, which have a P3HT/TiO_2 interpenetrating heterojunction structure by the insertion of the GQDs as anode buffer layers. Herein, we focus on function of the GQDs such as broadening the light absorption and engineering the energy level alignment of the BHJ, benefiting charge carrier transport, and eventually enhancing the PCE of HSCs.

RESULTS AND DISCUSSION

The top-down route from pulsed laser ablation in liquid (PLAL) is a clean, facile and versatile method to synthesize high quality GQDs, and the scheme is shown in Figure 1a. In a typical procedure, graphene nanosheets were first prepared and then used as targets for laser fragmentation. Figure 1b highlights the scanning electron microscopy (SEM) images of the grapheme sheets, that is high quality quadrate graphene sheets with heights within 3 nm, indicating that they consist of no more than three layers. After a few minutes of laser ablation, raw graphene nanosheets with sizes of tens of micrometers were dramatically cut to tiny fragments (Figure 1c). Different from ultrafast pulse methods such as femtosecond or picosecond laser pulse techniques, a long-pulse laser with pulse width of ~10 ns, which possesses rather low power densities, was applied, and this would cause strong linear absorption of the gaphene nanosheet and the subsequent Joule heating.[47,48] Besides, the graphene nanosheets have a black color that favors the absorption of 1064 nm laser power. Therefore, a large amount of heat accumulates quickly by continual irradiations, which will eventually cause the graphene nanosheets to break down into smaller pieces. Those large-size

DOI: 10.1021/sc500761n
ACS Sustainable Chem. Eng. 2015, 3, 637−644

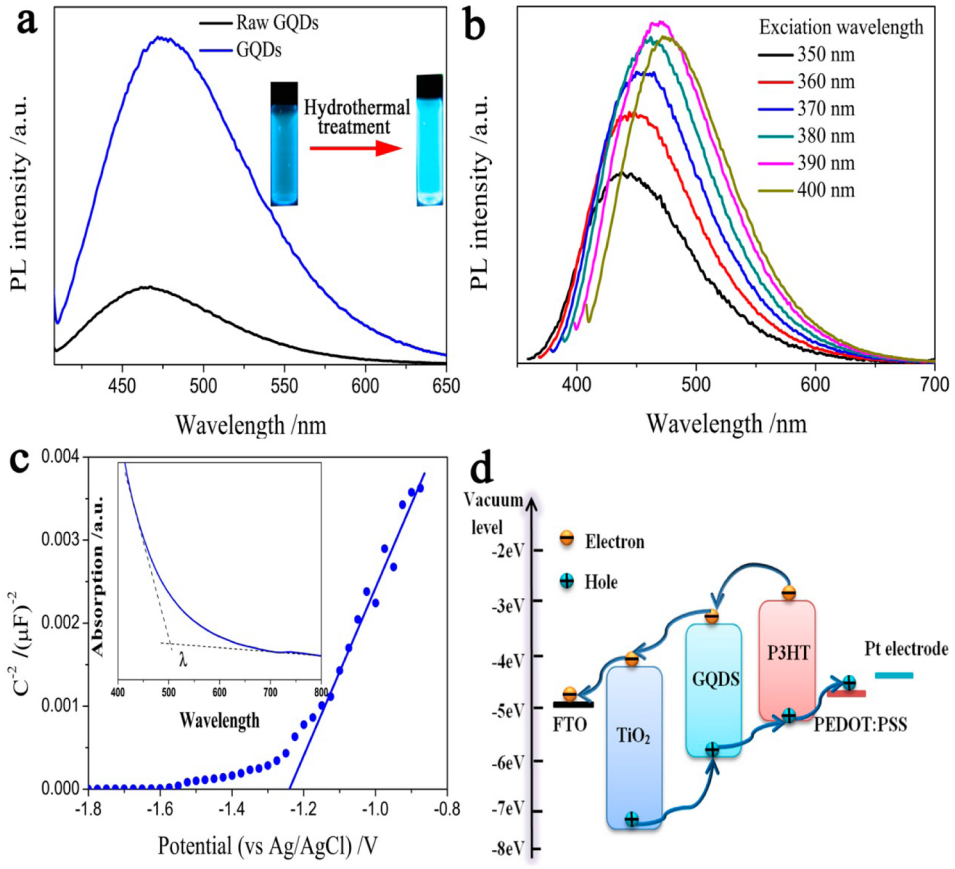

Figure 2. (a) PL spectra of the raw GQDs before and after hydrothermal treatment. Insert illustrates the photos of GQDs under ultraviolet irradiation. (b) PL spectra of the GQDs with different excitation wavelengths. (c) Mott−Schottky plots of the different GQD film at the frequency of 1 kHz in the aqueous solution of 0.05 M Na_2SO_4. Insert highlights the UV−vis absorption spectra of the GQDs. (d) Schematic configuration showing energy level diagram of each layer and the charge transfer process of the HSC with a GQD intermediate layer.

gaphene nanocrystals with band gaps smaller than the incident photon energy can be heated further until they break down into small pieces. Although the small-size gaphene nanosheets with wider band gaps are transparent to the incident laser pulses and remain intact. This selective breakdown mechanism benefits monodisperse QDs in a top-down way. As laser irradiation time extends, the average size of as-prepared GQDs reduced further and gone uniformly until reaching the limit after about 30 min. Figure 1a illustrates the photos of the graphene target solution and the graphene nanosheet after laser fragmentation process, and the graphene fragments dispersed in water after hydrothermal treatment. The solution was initially black in color, and then became light yellow in color after several minutes of laser irradiation, and finally turned to dark yellow, accordingly. It is worth mentioning that the hydrothermal method is an effectual synthetic route for the preparation of high quality GQDs. In this work, the usage of strong alkali (see the Experimental Section) as scissors to further cut the carbon based fragments into smaller colloid GQDs. Figure 1d shows the transmission electron microscopy (TEM) image of the GQDs. A narrow polydispersity of GQDs can be achieved after hydrothermal treatments as displayed. The statistical size distributions of the GQDs were roughly estimated from more than 100 nanoparticles from TEM images and the results are shown in Figure 1g. In detail, the diameters of the GQDs are mainly distributed in the range of 3.5−6.0 nm, indicating that the GQDs are highly monodisperse with average diameter of 4.8 nm (35%). Besides, the high-resolution transmission electron microscopy (TEM) image of an individual GQD is shown in Figure 1e. It reveals that the GQD is highly crystalline, and a lattice parameter is obtained to be 0.319 nm, which reasonably agrees with the results from the literature.[44,49] It seems that the zigzag orientation dominates the GQD edges, although other orientations are also possible. A schematic representation the structure of this GQD is shown in Figure 1f. It has been demonstrated that graphene with zigzag edges can offer unique electronic behaviors,[50,51] and we expect this GQDs could be used as a buffer layer to enhance device performance.

Under 375 nm ultraviolet light irradiation, the GQDs exhibited bright blue emission, as shown in the inset of Figure 2a. To further explore the optical properties of the GQDs, the PL spectra were measured for GQDs with the post hydrothermal treatment and the raw GQDs from laser ablation. The PL intensity is enhanced evidently after hydrothermal treatment, and this can be ascribed to the massive surface disorder or defects forming in the raw QDs during laser-induced breakdown process. These undesired surface defects may introduce unpredictable defect states which will result in deleterious nonradiational relaxations and quench the fluorescence.[52] However, the hydrothermal treatment can generate the high pressure with high temperature which could passivate the GQDs significantly, thus leading to brighter photoluminescence. The reformative GQDs exhibited an excitation-dependent PL behavior as shown in Figure 2b, which agreed well with previous reports.[53] The PL peak gradually shifted to longer wavelengths by altering the excitation wavelength from

DOI: 10.1021/sc500761n
ACS Sustainable Chem. Eng. 2015, 3, 637−644

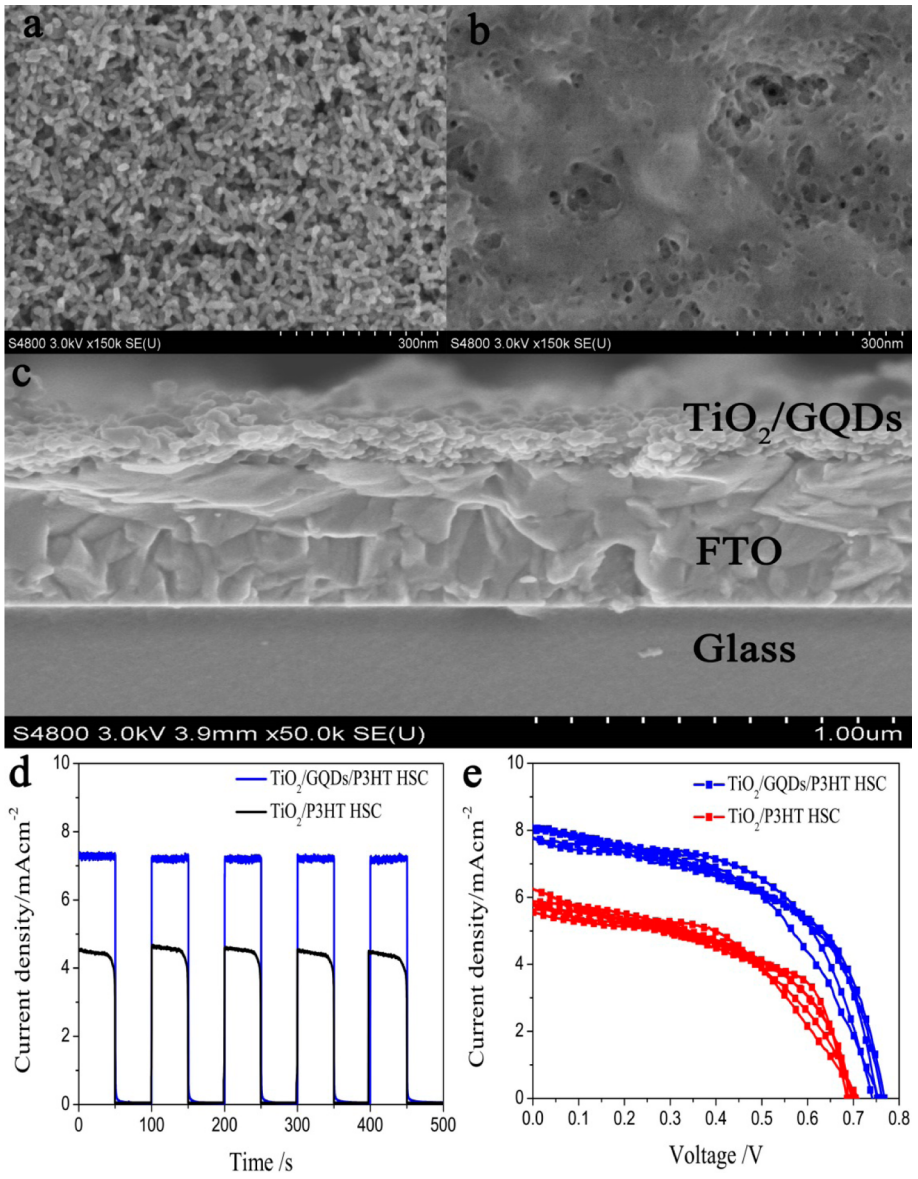

Figure 3. SEM images of TiO_2 (a) and TiO_2/GQDs (b). (c) Cross-sectional SEM image of TiO_2/GQDs blend film. (d) On−off switches by illuminating (100 mW cm^{-2}) and darkening (0 mW cm^{-2}). (e) $J-V$ curves of the HSCs with and without GQDs.

350 to 450 nm. This excitation-dependent PL peak shift is attributed to the inhomogeneities of the energy level which originates from the different sizes of the GQDs but also a distribution of different emissive states on individual passivated GQDs.

The energy level formation between the donor and acceptor is one of the important determinants of the device performances.[54−56] Previous efforts have attempted to tune the electronic activities of the acceptor (TiO_2) by utilizing active ion dopants.[57,58] In this work, an intermediate GQD layer was employed to improve the energy level formation of the donor−acceptor system. To obtain absolute bandedge positions of the GQDs, the Mott−Schottky plots measurements were performed to determine the flat band potentials of the QD films. Figure 2c shows the Mott−Schottky plots of the GQDs, that is, $1/C^2$ as a function of electrochemical potentials, where the capacitance C is obtained from the impedance measurement.[59] Positive slopes of Mott−Schottky plots indicate that the GQDs are n-type. The conduction band (CB) energy level was calculated with Ag/Ag^+ as the reference. The ferrocene ($E_{1/2}$ vs Ag/Ag^+ = 0.09 eV) potential as a standard should be measured in the electrolyte solution using the same reference electrode, and −4.80 eV fixed as an energy level in the vacuum set. Finally, the energy levels of CB can be calculated using the following formula: CB (eV) = $-4.8 - (E - E_{1/2})$ (eV),[60] where E is the intercept at the x-axis, $E_{1/2}$ is the ferrocene potential used as a standard, $E_{1/2}$ vs Ag/Ag^+ = 0.09 eV. As a result, the CB level of the GQD was obtained to be −3.47 eV and the band gap was determined to be 2.47 eV from the UV−vis absorption spectrum (inset in Figure 2c) using the following relationship: Eg = $1240/\lambda$ eV. Finally, the valence band (VB) energy level was obtained, i.e., −5.94 eV. The CB, VB and Eg values are in reasonable agreement with those GQDs obtained from double-walled carbon nanotubes,[49] indicating that the results obtained in this work are reliable. The CB edge position of the GQDs is located above that of TiO_2, indicating that these GQDs are electronically active for transport photoexcited electrons. Besides, the cascade energy level architecture was established

DOI: 10.1021/sc500761n
ACS Sustainable Chem. Eng. 2015, 3, 637−644

Table 1. Photovoltaic Parameters of the HSCs

HSC	V_{oc} [V]	J_{sc} [mA·cm^{-2}]	FF	η^a [%]
TiO_2/P3HT	0.698 ± 0.011	5.89 ± 0.25	0.50 ± 0.01	2.04 ± 0.05
TiO_2/GQDs/P3HT	0.757 ± 0.009	7.98 ± 0.18	0.52 ± 0.02	3.16 ± 0.05

$^a\eta = J_{sc}V_{oc}FF/P_{in}$, where P_{in} = 100 mw·cm^{-2} (AM 1.5).

after the insertion of GQD intermediate layer as shown in Figure 2d. The energy offset was apparently lowered by the cascade small offsets in TiO_2/GQDs/P3HT junctions comparing to TiO_2/P3HT system, which might benefit the charge transfer and funnel the charge carriers to the circuit.[61]

The photoexcited electron transfer can be roughly evaluated by the steady-state PL measurements of P3HT layer when it is coupled with an appropriate electron- or hole-extraction layer. To reveal the role of GQDs that play on charge transfer properties at the interface of acceptor−donor BHJs, the steady state PL spectra were measured for P3HT, TiO_2/P3HT and TiO_2/GQDs/P3HT films, as shown in Figure S1 (Supporting Information). An efficient PL quenching is indicative of a higher degree of the photoinduced electron transfer in TiO_2/GQDs/P3HT than its counterpart TiO_2/P3HT. This suggests that GQDs are capable of charge transfer in the hybrid BHJ. This enhanced charge transfer for TiO_2/GQDs/P3HT blend film on one hand may be ascribed to the better occupation redundant space or pores by the incorporation of GQDs, thus favoring the physical adsorptions of P3HT molecules in virtue of intermolecular attractive forces and forming intimate contact between P3HT molecules and acceptor. On the other hand, GQDs with adequate energy level positions between the donor and acceptor may provide better channels that benefit the photoexcited charge transfer. Figure S2 (Supporting Information) shows the UV−vis absorption spectra of the pure P3HT and P3HT/GQDs (weight ratio 1:1) films. The absorption intensity was normalized by the film thickness. It is apparent that the absorption intensity of the P3HT/GQDs film is slightly higher than that of the pure P3HT film in the wavelength region of 450−600 nm. The increase of the absorbance around 500 nm can be ascribed to the strong characteristic absorption of GQDs, which is consistent with the band gap of GQDs (2.4 eV). Therefore, a GQD buffer layer with the appropriate absorption range can cooperate with P3HT to achieve a better match with the solar spectrum and enhance spectral coverage.

In a bid to explore the effect of intermediate GQD layer on the final photovoltaic performance, two types of solar cells were fabricated for comparison: TiO_2/P3HT and TiO_2/GQDs/P3HT HSCs. Figure 3a shows the morphology of the TiO_2 layer, which reveals that the prepared acceptor layer clearly exhibits a porous structure, thus favoring the physical adsorption of GQDs by trapping the molecules in the microporomerics. After 4 h of soaking, the GQDs were well permeated into the acceptor, and a uniformly layer was covered on the TiO_2 acceptor layer, as shown in Figure 3b. It is known that the intimate interface contact is essential for efficient exciton separation because the photoexcited excitons in P3HT cannot diffuse too long, typically ∼12 nm.[62] As observed from Figure S3a (Supporting Information), the surface of the prepared TiO_2 acceptor layers clearly exhibits a porous structure, which favors the physical adsorption by trapping the solution in the microporomerics because of the intermolecular attractive forces. The cross-section of the TiO_2/GQDs reveals that the excellent interface contact was formed, as shown in Figure 3c. It is worth mentioning that the P3HT and TiO_2 still exhibit intimate interface contact after incorporation of GQDs, as demonstrated in Figure S3b (Supporting Information). The intimate interface favors the efficient charge separation,[63] and the thickness of TiO_2/GQDs layer was estimated to be about 250 nm. A robust solar panel also requires fast start-up, multiple start/stop cycling and a stable photocurrent as well. Figure 3d shows the start−stop switches for the devices with and without GQDs. The cell with GQDs delivers a faster start-up and turn-off time than its counterpart, implying that the GQD intermediate layer is vigorous in transporting charge carriers. During the irradiation in each "on" state, the photocurrent density remained unchanged in HSC with GQDs, whereas attenuation in photocurrent density was observed in its counterpart. This suggests that introducing of GQDs provides better channels for the photoexcited charge carrier transfer and can suppress those undesired electron−hole recombinations. The photocurrent−voltage (J−V) curves of the TiO_2/P3HT and TiO_2/GQDs/P3HT HSCs under a simulated solar light irradiation of 100 mW cm^{-2} are shown in Figure 3d. Each type of the HSCs was tested for five times under identical experimental conditions, and the statistic of the device parameters with standard derivations are listed in Table 1. After introduction of the GQDs buffer layer, the short-circuit current density J_{sc} increases from 5.89 to 7.98 mA·cm^{-2}. Meanwhile, the open-circuit voltage V_{oc} increases from 0.698 to 0.757 V, thus leading to a notable PCE enhancement, i.e., from 2.04 to 3.16%. The PCE of the ternary GQDs-based HSC is much higher than that of the conventional device with TiO_2/P3HT architecture, which must be attributed to the presence of the GQDs in the active layer. After introduction of the GQDs buffer layer, the energy offset between the donor and acceptor is greatly reduced, and this favors the transport of the photoexcited holes and electrons. In addition, GQDs enables the directly harvest high energy photons due to its the larger band gap, which is a complementarity to the insufficient capturing energetic photons for pure P3HT.

CONCLUSIONS

In summary, GQDs with a bright blue emission were fabricated by laser fragmentation of graphene sheet solution with post hydrothermal treatment. The prepared GQDs exhibited a moderate bad gap with CB level above TiO_2 and below that of P3HT. GQDs were incorporated into the hybrid heterojunction as intermediate buffer layer to form cascade energy level architecture. The ternary blends delivered a higher PCE of 3.16% as compared to the conventional TiO_2/P3HT device, i.e., 2.04%. On one hand, the ternary bulk heterojuction enhanced harvest of the high energy photons. On the other hand, the unique band structure of the GQDs funneled the photoexcited charge carriers in a direct flow to the circuit. Although this work is far from being optimized, these profound advantages, along with ease of fabrication, low toxicity and scalable in tuning the electronic structures, provide a promising candidate buffer material for photovoltaic applications.

DOI: 10.1021/sc500761n
ACS Sustainable Chem. Eng. 2015, 3, 637−644

EXPERIMENTAL SECTION

Preparation of Graphene Nanosheets. Graphene nanosheets were prepared by the ultrasonication powdering method, which has been elaborated in previous reports. The resulting graphene slices were purified by abstersion, centrifugation and redispersion in distilled water. This cleaning process was repeated twice, then dried with nitrogen flow and stored with solid form in a nitrogen-filled glovebox.

Top-down Route for GQDs. A 1064 nm pulsed laser beam with pulse width of 10 ns (fwhm) is generated by a frequency-doubled and Q-switched neodymium doped yttrium aluminum garnet laser, operating at 10 Hz, pulse energy 35 μJ per pulse. A spatial filter was used to modulate the spatial distribution for compensating the instability of the laser's resonator, and the obtained pulse was nearly Gaussian profile. The laser beam was tightly focused by a convex lens with a focal length of 400 mm, and the irradiance of beam at the focus was estimated to be about 20 μm. Black graphene nanosheet aqueous solution (3.0 mg/mL) was first poured into a quartz cell. The cell was fixed at the focal point on a three-dimensional mobile platform. To gain better uniformity of the laser ablation, the platform was controlled to change the irradiated spot every 10 incident pulses. Besides, a magnetic stirrer was used to keep graphene nanosheets fully suspended in the solution during laser irradiation. The whole setup could guarantee a highly efficient laser fragmentation. The laser irradiation lasted for 40 min until a light yellow solution was observed. Raw GQDs were separated from the precipitate (i.e., the large size graphene nanocrystals) by centrifugation to obtain the retrieved transparent solution with raw GQDs. After that, the PH of raw GQD solution was adjusted to 9 with NaOH solution. Subsequently, the mixture was diluted with deionized water (60 mL) and hydrothermally treated in an autoclave at 150 °C for 12 h to form a dark yellow GQD solution.

Fabricaiton of HSCs. The TiO_2 colloid was prepared by the procedure in a similar way as done in our previous works.[32,33] A layer of acceptor film with a thickness of about 250 nm was prepared by coating the TiO_2 colloid on FTO glass using a spin-coating technique, followed by sintering in air at 450 °C for 30 min. Then the acceptor film was soaked in 10 mg/mL GQD aqueous solution for 4 h to uptake the GQDs. After that, a 0.15 M conjugated polymer P3HT methylbenzene solution was spin-coated on the top of TiO_2/GQDs layer to form a tenry bulk heterojunction. Next, the PEDOT:PSS layer was spin-coated onto the BHJ. Finally, Pt electrodes were deposited on the top of the PEDOT:PSS layer by thermal evaporation under vacuum. The active area of the solar cell device is about 0.25 cm^2.

Characterizations. The morphology of acceptor layers was characterized by using field emission scanning electron microscopy (FE-SEM, Hitachi S4800). The samples for cross-sectional SEM characterizations were prepared by breaking a HSC anode in half. Mott−Schottky measurements were done at the frequency of 1 kHz in the aqueous solution of 0.05 M Na_2SO_4 using a BAS 100B instrument and Ag/AgCl electrode as the reference electrode. The photoluminescence (PL) spectrum was measured by using a spectrophotometer (FLS920, Edinburgh), in which a xenon lamp and a photomultiplier tube (R955, Hamamatsu) were used as excitation source and fluorescence detector, respectively. UV−vis absorption spectra were recorded with a Varian Cary 300 spectrophotometer. The photocurrent−voltage (J−V) curves of the assembled HSCs were recorded on an Electrochemical Workstation (Xe Lamp Oriel Sol_3A Class AAA Solar Simulators 94023A, USA) under the irradiation of a simulated solar light from a 100 W xenon arc lamp in ambient atmosphere, which was calibrated using a Newport-certified single crystal Si solar cell.

ASSOCIATED CONTENT

Supporting Information

Time-integrated PL spectra for P3HT, TiO_2/P3HT and TiO_2/GQDs/P3HT films, absorption spectra for P3HT and GQDs/P3HT films and cross-sectional SEM images of bare TiO_2 and TiO_2/GQDs/P3HT BHJ. This material is available free of charge via the Internet at http://pubs.acs.org.

AUTHOR INFORMATION

Corresponding Authors

*Q. Li. E-mail: qhli@hqu.edu.cn.
*Y. Qin. E-mail: qinyuancheng@hotmail.com.
*X. Jin. E-mail: siaojin@163.com.

Notes

The authors declare no competing financial interest.

ACKNOWLEDGMENTS

The authors gratefully acknowledge the financial support of the Natural Science Foundation of China (61366003), the Science and Technology Project of the Education Department of Jiangxi Province, China (GJJ13474, GJJ14533), the Aviation Science Fund of China (2013ZF56025) and the Natural Science Foundation of Jiangxi Province (20142BAB213015).

REFERENCES

(1) Graetzel, M.; Janssen, R. A.; Mitzi, D. B.; Sargent, E. H. Materials interface engineering for solution-processed photovoltaics. *Nature* **2012**, *488*, 304−312.
(2) Lei, Y.; Jia, H.; He, W.; Zhang, Y.; Mi, L.; Hou, H.; Zhu, G.; Zheng, Z. Hybrid solar cells with outstanding short-circuit currents based on a room temperature soft-chemical strategy: The case of P3HT:Ag_2S. *J. Am. Chem. Soc.* **2012**, *134*, 17392−17395.
(3) Liu, Y.; Summers, M. A.; Edder, C.; Fréchet, J. M. J.; McGehee, M. D. Using resonance energy transfer to improve exciton harvesting in organic-inorganic hybrid photovoltaic cells. *Adv. Mater.* **2005**, *17*, 2960−2964.
(4) Reeja-Jayan, B.; Manthiram, A. Influence of polymer-metal interface on the photovoltaic properties and long-term stability of nc-TiO_2-P3HT hybrid solar cells. *Sol. Energy Mater. Sol. Cells* **2010**, *94*, 907−914.
(5) Gao, F.; Ren, S.; Wang, J. The renaissance of hybrid solar cells: Progresses, challenges, and perspectives. *Energy Environ. Sci.* **2013**, *6*, 2020−2040.
(6) Shoaee, S.; Briscoe, J.; Durrant, J. R.; Dunn, S. Acoustic enhancement of polymer/ZnO nanorod photovoltaic device performance. *Adv. Mater.* **2014**, *26*, 263−268.
(7) Lee, J.; Mubeen, S.; Hernandez-Sosa, G.; Sun, Y.; Toma, F. M.; Stucky, G. D.; Moskovits, M. High-efficiency panchromatic hybrid Schottky solar cells. *Adv. Mater.* **2013**, *25*, 256−260.
(8) Wang, X.; Ishwara, T.; Gong, W.; Campoy-Quiles, M.; Nelson, J.; Bradley, D. D. C. High-performance metal-free solar cells using stamp transfer printed vapor phase polymerized poly(3,4-ethylenedioxythiophene) top anodes. *Adv. Funct. Mater.* **2012**, *22*, 1454−1460.
(9) Roberson, L. B.; Poggi, M. A.; Kowalik, J.; Smestad, G. P.; Bottomley, L. A.; Tolbert, L. M. Correlation of morphology and device performance in inorganic-organic TiO_2-polythiophene hybrid solid-state solar cells. *Coord. Chem. Rev.* **2004**, *248*, 1491−1499.
(10) Jin, X.; Sun, W.; Chen, Z.; Li, Y.; Li, P.; He, X.; Yuan, Y.; Zou, S.; Qin, Y.; Li, Q. Efficient electron/hole transport in inorganic/organic hybrid solar cells by lithium ion and molybdenum trioxide codoping. *J. Power Sources* **2014**, *268*, 874−881.
(11) Kong, D.; Jin, X.; Sun, W.; Du, J.; Tong, J.; Chen, C.; Yang, X.; Cheng, Y.; Li, Q. Ruthenium cation substitutional doping for efficient charge carrier transfer in organic/inorganic hybrid solar cells. *J. Power Sources* **2015**, *274*, 701−708.
(12) Kroon, R.; Lenes, M.; Hummelen, J. C.; Blom, P. W. M.; de Boer, B. Small bandgap polymers for organic solar cells (polymer material development in the last 5 years). *Polym. Rev.* **2008**, *48*, 531−582.
(13) Heo, S. W.; Song, I. S.; Kim, Y. S.; Moon, D. K. Fabrication of OPVs by introducing a conductivity-enhanced hybrid buffer layer. *Sol. Energy Mater. Sol. Cells* **2012**, *101*, 295−302.

DOI: 10.1021/sc500761n
ACS Sustainable Chem. Eng. 2015, 3, 637−644

(14) Li, P.; Li, X.; Sun, C.; Wang, G.; Li, J.; Jiu, T.; Fang, J. Performance enhancement of inverted polymer solar cells with fullerene ester derivant-modified ZnO film as cathode buffer layer. *Sol. Energy Mater. Sol. Cells* **2014**, *126*, 36−41.
(15) Albrecht, S.; Grootoonk, B.; Neubert, S.; Roland, S.; Wördenweber, J.; Meier, M.; Schlatmann, R.; Gordijn, A.; Neher, D. Efficient hybrid inorganic/organic tandem solar cells with tailored recombination contacts. *Sol. Energy Mater. Sol. Cells* **2014**, *127*, 157−162.
(16) Park, J. H.; Lee, T. W.; Chin, B. D.; Wang, D. H.; Park, O. O. Roles of interlayers in efficient organic photovoltaic devices. *Macromol. Rapid Commun.* **2010**, *31*, 2095−2108.
(17) Luo, J.; Im, J. H.; Mayer, M. T.; Schreier, M.; Nazeeruddin, M. K.; Park, N. G.; Tilley, S. D.; Fan, H. J.; Gratzel, M. Water photolysis at 12.3% efficiency via perovskite photovoltaics and earth-abundant catalysts. *Science* **2014**, *345*, 1593−1596.
(18) Choi, M. R.; Han, T. H.; Lim, K. G.; Woo, S. H.; Huh, D. H.; Lee, T. W. Soluble self-doped conducting polymer compositions with tunable work function as hole injection/extraction layers in organic optoelectronics. *Angew. Chem., Int. Ed.* **2011**, *50*, 6274−6277.
(19) Lim, K.-G.; Choi, M.-R.; Kim, H.-B.; Park, J. H.; Lee, T.-W. High-efficiency polymer photovoltaic cells using a solution-processable insulating interfacial nanolayer: The role of the insulating nanolayer. *J. Mater. Chem.* **2012**, *22*, 25148.
(20) Lee, T.-W.; Lim, K.-G.; Kim, D.-H. Approaches toward efficient and stable electron extraction contact in organic photovoltaic cells: Inspiration from organic light-emitting diodes. *Electron. Mater. Lett.* **2010**, *6*, 41−50.
(21) Chen, L.; Wang, P.; Li, F.; Yu, S.; Chen, Y. Efficient bulk heterojunction polymer solar cells using PEDOT/PSS doped with solution-processed MoO_3 as anode buffer layer. *Sol. Energy Mater. Sol. Cells* **2012**, *102*, 66−70.
(22) Mohd Yusoff, A. R. b.; Kim, H. P.; Jang, J. Organic photovoltaics with V_2O_5 anode and ZnO nanoparticles cathode buffer layers. *Org. Electron.* **2013**, *14*, 858−861.
(23) Cheng, F.; Fang, G.; Fan, X.; Liu, N.; Sun, N.; Qin, P.; Zheng, Q.; Wan, J.; Zhao, X. Enhancing the short-circuit current and efficiency of organic solar cells using MoO_3 and CuPc as buffer layers. *Sol. Energy Mater. Sol. Cells* **2011**, *95*, 2914−2919.
(24) Wang, H.-Q.; Stubhan, T.; Osvet, A.; Litzov, I.; Brabec, C. J. Up-conversion semiconducting MoO_3:Yb/Er nanocomposites as buffer layer in organic solar cells. *Sol. Energy Mater. Sol. Cells* **2012**, *105*, 196−201.
(25) Bernède, J. C.; Cattin, L.; Makha, M.; Jeux, V.; Leriche, P.; Roncali, J.; Froger, V.; Morsli, M.; Addou, M. MoO_3/CuI hybrid buffer layer for the optimization of organic solar cells based on a donor−acceptor triphenylamine. *Sol. Energy Mater. Sol. Cells* **2013**, *110*, 107−114.
(26) Liu, J.; Shao, S.; Fang, G.; Wang, J.; Meng, B.; Xie, Z.; Wang, L. High-efficiency inverted tandem polymer solar cells with step-Al-doped MoO_3 interconnection layer. *Sol. Energy Mater. Sol. Cells* **2014**, *120*, 744−750.
(27) Shen, L.; Xu, Y.; Meng, F.; Li, F.; Ruan, S.; Chen, W. Semitransparent polymer solar cells using V_2O_5/Ag/V_2O_5 as transparent anodes. *Org. Electon.* **2011**, *12*, 1223−1226.
(28) Wang, H.-Q.; Li, N.; Guldal, N. S.; Brabec, C. J. Nanocrystal V_2O_5 thin film as hole-extraction layer in normal architecture organic solar cells. *Org. Electron.* **2012**, *13*, 3014−3021.
(29) Lee, S. J.; Pil Kim, H.; Mohd Yusoff, A. R. b.; Jang, J. Organic photovoltaic with PEDOT:PSS and V_2O_5 mixture as hole transport layer. *Sol. Energy Mater. Sol. Cells* **2014**, *120*, 238−243.
(30) Bian, H. Q.; Ma, S. Y.; Zhang, Z. M.; Gao, J. M.; Zhu, H. B. Microstructure and Raman scattering of Ag-doping ZnO films deposited on buffer layers. *J. Cryst. Growth* **2014**, *394*, 132−136.
(31) Yu, X.; Yu, X.; Zhang, J.; Hu, Z.; Zhao, G.; Zhao, Y. Effective light trapping enhanced near-UV/blue light absorption in inverted polymer solar cells via sol−gel textured Al-doped ZnO buffer layer. *Sol. Energy Mater. Sol. Cells* **2014**, *121*, 28−34.
(32) Jin, X.; Li, Q.; Li, Y.; Chen, Z.; Wei, T. H.; He, X.; Sun, W. Energy level control: Toward an efficient hot electron transport. *Sci. Rep.* **2014**, *4*, 5983.
(33) Li, Q.; Jin, X.; Yang, X.; Chen, C.; Chen, Z.; Qin, Y.; Wei, T.-h.; Sun, W. Reducing the excess energy offset in organic/inorganic hybrid solar cells: Toward faster electron transfer. *Appl. Catal., B* **2015**, *162*, 524−531.
(34) Jin, X.; Sun, W.; Chen, Z.; Wei, T.; Chen, C.; He, X.; Yuan, Y.; Li, Y.; Li, Q. Exciton generation/dissociation/charge-transfer enhancement in inorganic/organic hybrid solar cells by robust single nanocrystalline LnP_xO_y (Ln = Eu, Y) doping. *ACS Appl. Mater. Interfaces* **2014**, *6*, 8771−8781.
(35) Sargent, E. H. Colloidal quantum dot solar cells. *Nat. Photonics* **2012**, *6*, 133−135.
(36) Darling, S. B.; You, F.; Veselka, T.; Velosa, A. Assumptions and the levelized cost of energy for photovoltaics. *Energy Environ. Sci.* **2011**, *4*, 3133−3139.
(37) Darling, S. B.; You, F. The case for organic photovoltaics. *RSC Adv.* **2013**, *3*, 17633−17648.
(38) Deutsch, Z.; Neeman, L.; Oron, D. Luminescence upconversion in colloidal double quantum dots. *Nat. Nanotechnol.* **2013**, *8*, 649−653.
(39) Sun, L.; Koh, Z. Y.; Wang, Q. PbS quantum dots embedded in a ZnS dielectric matrix for bulk heterojunction solar cell applications. *Adv. Mater.* **2013**, *25*, 4598−4604.
(40) Tabachnyk, M.; Ehrler, B.; Gélinas, S.; Böhm, M. L.; Walker, B. J.; Musselman, K. P.; Greenham, N. C.; Friend, R. H.; Rao, A. Resonant energy transfer of triplet excitons from pentacene to PbSe nanocrystals. *Nat. Mater.* **2014**, *13*, 1033−1038.
(41) Dong, Y.; Lin, J.; Chen, Y.; Fu, F.; Chi, Y.; Chen, G. Graphene quantum dots, graphene oxide, carbon quantum dots and graphite nanocrystals in coals. *Nanoscale* **2014**, *6*, 7410−7415.
(42) Li, L.; Wu, G.; Yang, G.; Peng, J.; Zhao, J.; Zhu, J. J. Focusing on luminescent graphene quantum dots: Current status and future perspectives. *Nanoscale* **2013**, *5*, 4015−4039.
(43) Sun, H.; Wu, L.; Wei, W.; Qu, X. Recent advances in graphene quantum dots for sensing. *Mater. Today* **2013**, *16*, 433−442.
(44) Peng, J.; Gao, W.; Gupta, B. K.; Liu, Z.; Romero-Aburto, R.; Ge, L.; Song, L.; Alemany, L. B.; Zhan, X.; Gao, G.; Vithayathil, S. A.; Kaipparettu, B. A.; Marti, A. A.; Hayashi, T.; Zhu, J. J.; Ajayan, P. M. Graphene quantum dots derived from carbon fibers. *Nano Lett.* **2012**, *12*, 844−849.
(45) Han, T.-H.; Lee, Y.; Choi, M.-R.; Woo, S.-H.; Bae, S.-H.; Hong, B. H.; Ahn, J.-H.; Lee, T.-W. Extremely efficient flexible organic light-emitting diodes with modified graphene anode. *Nat. Photonics* **2012**, *6*, 105−110.
(46) Kwon, W.; Kim, Y.-H.; Lee, C.-L.; Lee, M.; Choi, H. C.; Lee, T.-W.; Rhee, S.-W. Electroluminescence from graphene quantum dots prepared by amidative cutting of tattered graphite. *Nano Lett.* **2014**, *14*, 1306−1311.
(47) Yang, J.; Ling, T.; Wu, W. T.; Liu, H.; Gao, M. R.; Ling, C.; Li, L.; Du, X. W. A top-down strategy towards monodisperse colloidal lead sulphide quantum dots. *Nat. Commun.* **2013**, *4*, 1695.
(48) Werner, D.; Hashimoto, S. Improved working model for interpreting the excitation wavelength- and fluence-dependent response in pulsed laser-induced size reduction of aqueous gold nanoparticles. *J. Phys. Chem. C* **2010**, *115*, 5063−5072.
(49) Li, F.; Kou, L.; Chen, W.; Wu, C.; Guo, T. Enhancing the short-circuit current and power conversion efficiency of polymer solar cells with graphene quantum dots derived from double-walled carbon nanotubes. *NPG Asia Mater.* **2013**, *5*, e60.
(50) Radovic, L. R.; Bockrath, B. On the chemical nature of graphene edges: Origin of stability and potential for magnetism in carbon materials. *J. Am. Chem. Soc.* **2005**, *127*, 5917−5927.
(51) Gusynin, V. P.; Miransky, V. A.; Sharapov, S. G.; Shovkovy, I. A.; Wyenberg, C. M. Edge states on graphene ribbons in magnetic field: Interplay between Dirac and ferromagnetic-like gaps. *Phys. Rev. B* **2009**, *79*, 115431.

DOI: 10.1021/sc500761n
ACS Sustainable Chem. Eng. 2015, 3, 637−644

(52) Zhang, H.; Wang, L.; Xiong, H.; Hu, L.; Yang, B.; Li, W. Hydrothermal synthesis for high-quality CdTe nanocrystals. *Adv. Mater.* **2003**, *15*, 1712−1715.
(53) Sun, Y.-P.; Zhou, B.; Lin, Y.; Wang, W.; Fernando, K. A. S.; Pathak, P.; Meziani, M. J.; Harruff, B. A.; Wang, X.; Wang, H.; Luo, P. G.; Yang, H.; Kose, M. E.; Chen, B.; Veca, L. M.; Xie, S.-Y. Quantum-sized carbon dots for bright and colorful photoluminescence. *J. Am. Chem. Soc.* **2006**, *128*, 7756−7757.
(54) Li, W.; Roelofs, W. S.; Wienk, M. M.; Janssen, R. A. Enhancing the photocurrent in diketopyrrolopyrrole-based polymer solar cells via energy level control. *J. Am. Chem. Soc.* **2012**, *134*, 13787−13795.
(55) Scharber, M. C.; Mühlbacher, D.; Koppe, M.; Denk, P.; Waldauf, C.; Heeger, A. J.; Brabec, C. J. Design rules for donors in bulk-heterojunction solar cells—Towards 10% energy-conversion efficiency. *Adv. Mater.* **2006**, *18*, 789−794.
(56) Rand, B.; Burk, D.; Forrest, S. Offset energies at organic semiconductor heterojunctions and their influence on the open-circuit voltage of thin-film solar cells. *Phys. Rev. B* **2007**, *75*, 115327.
(57) Li, Q.; Yuan, Y.; Wei, T.; Li, Y.; Chen, Z.; Jin, X.; Qin, Y.; Sun, W. The origin of efficiency enhancement of inorganic/organic hybrid solar cells by robust samarium phosphate nanophosphors. *Sol. Energy Mater. Sol. Cells* **2014**, *130*, 426−434.
(58) Jin, X.; Sun, W.; Chen, C.; Wei, T.; Cheng, Y.; Li, P.; Li, Q. Efficiency enhancement via tailoring energy level alignment induced by vanadium ion doping in organic/inorganic hybrid solar cells. *RSC Adv.* **2014**, *4*, 46008−46015.
(59) Liao, L.; Zhang, Q.; Su, Z.; Zhao, Z.; Wang, Y.; Li, Y.; Lu, X.; Wei, D.; Feng, G.; Yu, Q.; Cai, X.; Zhao, J.; Ren, Z.; Fang, H.; Robles-Hernandez, F.; Baldelli, S.; Bao, J. Efficient solar water-splitting using a nanocrystalline CoO photocatalyst. *Nat. Nanotechnol.* **2014**, *9*, 69−73.
(60) Li, Y. C.; Zhong, H. Z.; Li, R.; Zhou, Y.; Yang, C. H.; Li, Y. F. High-yield fabrication and electrochemical characterization of tetrapodal CdSe, CdTe, and $CdSe_xTe_{1-x}$ nanocrystals. *Adv. Fuct. Mater.* **2006**, *16*, 1705−1716.
(61) Yang, B.; Yuan, Y.; Sharma, P.; Poddar, S.; Korlacki, R.; Ducharme, S.; Gruverman, A.; Saraf, R.; Huang, J. Tuning the energy level offset between donor and acceptor with ferroelectric dipole layers for increased efficiency in bilayer organic photovoltaic cells. *Adv. Mater.* **2012**, *24*, 1455−1460.
(62) Shaw, P. E.; Ruseckas, A.; Samuel, I. D. W. Exciton diffusion measurements in poly(3-hexylthiophene). *Adv. Mater.* **2008**, *20*, 3516−3520.
(63) Zhitomirsky, D.; Voznyy, O.; Hoogland, S.; Sargent, E. H. Measuring charge carrier diffusion in coupled colloidal quantum dot solids. *ACS Nano* **2013**, *7*, 5282−5290.

DOI: 10.1021/sc500761n
ACS Sustainable Chem. Eng. 2015, 3, 637−644